Catalysis Today 146 (2009) 63–70

Contents lists available at ScienceDirect

Catalysis Today

journal homepage: www.elsevier.com/locate/cattod

Ethanol steam reforming on Mg- and Ca-modified Cu–Ni/SBA-15 catalysts

A.J. Vizcaíno *, A. Carrero, J.A. Calles

Department of Chemical and Environmental Technology, ESCET, Rey Juan Carlos University, c/Tulipán, s/n, 28933 Móstoles, Spain

ARTICLE INFO

Article history:
Available online 17 January 2009

Keywords:
Ethanol steam reforming
Cu–Ni catalysts
SBA-15
Magnesium
Calcium
Promoting agents

ABSTRACT

The effect of Mg and Ca incorporation (0–20 wt%) into CuNi/SBA-15 catalysts for hydrogen production by ethanol steam reforming has been studied. Promoting elements, Ca and Mg, were added to SBA-15 support prior to the active phase, Cu (2 wt%) and Ni (7 wt%). In both cases, the metals were incorporated to SBA-15 by incipient wetness impregnation followed by calcination to obtain the corresponding oxides. XRD analyses and TEM images demonstrated that CaO and MgO improved the dispersion of the Cu–Ni phase. Moreover, TPR profiles showed that Ca or Mg strengthened the interaction between the SBA-15 support and the Cu–Ni phase. Both promoting effects of Ca and Mg, together with their basic character enhanced the catalytic performance of CuNi/SBA-15 catalysts on ethanol steam reforming, giving higher hydrogen selectivity and lower coke deposition.

1. Introduction

Owing to the global economic growth, population increase and technological development, the world primary energy demand, currently dominated by fossil fuels in more than 80%, is projected to expand by 53% from 2004 to 2030, reaching 17.1 billion tonnes of oil equivalent [1]. According to the International Energy Agency, if the situation does not change, it is estimated that global carbon dioxide emissions will increase by 1.7% per year, reaching 40 Gt/year in 2030. This would result in critical environmental problems all over the world [2]. In accordance with the Intergovernmental Panel on Climate Change (IPCC) [3], to stabilize carbon dioxide concentration into atmosphere in 550 ppm, it is necessary to obtain a reduction in carbon dioxide emissions of 50–60% before 2050. The use of hydrogen as an energy vector is an interesting and promising challenge. Hydrogen can be renewably produced in several ways and its utilization to obtain energy generates just water and no pollutant emission.

In this sense, ethanol has demonstrated to have good properties for hydrogen production [4]. Moreover, ethanol brings about a series of advantages, mainly handling safety and a renewable origin, as it can be produced in high amounts from several biomass sources (sugar and starchy crops, agricultural residues, wood and municipal solid wastes) [5]. Besides, the use of ethanol may avoid inconveniences of fossil fuels reserves, such as their limitation and location in politically unstable areas. Therefore, among the several ways to obtain hydrogen, ethanol steam reforming has become an interesting alternative for hydrogen production. This process, represented in Eq. (1), consists of a complex network of reactions giving hydrogen and several by-products as ethylene, acetaldehyde, methane, carbon oxides, coke, etc. Among undesirable products, it is necessary to stand out carbon monoxide and coke, as they cause poisoning of fuel cells and reforming catalysts.

$$C_2H_5OH + 3H_2O \rightarrow 2CO_2 + H_2 \quad (\Delta H^\circ_{298} = +347.4\,\text{kJ/mol}) \qquad (1)$$

The use of an appropriate catalyst may favour reaction pathways that minimize the formation of undesirable compounds, enhancing selectivity towards main products [4]. Regarding the active phase, supported Co, Rh or Ni catalysts are the most commonly used. Nickel catalysts possess high activity and low cost as advantages [4], but they produce high amounts of deposited coke. According to several studies, coke formation on Ni catalysts is related to the formation of large ensembles of metal atoms [6], but small additions of other metals, such as Au [7] or Cu [8], enhance Ni dispersion and reduce carbon deposition. Concretely, Cu–Ni supported catalysts have shown good catalytic properties for ethanol steam reforming [8–18], but coke deposition is still the major drawback for Cu–Ni catalysts.

Apart from the catalyst active phase, the support plays an important role, on metal dispersion, distribution and also on the reaction pathway. In this sense, it is well known that acid supports favour ethanol dehydration to ethylene, which easily may be transformed into coke [6,8,19]. According to the above-mentioned comments, there are some strategies to improve the catalyst performance and reduce the amount of carbon deposited:

(i) Reducing the metallic phase particles size, which means both higher active surface area and preferential elimination of large Cu–Ni ensembles related to coke deposition and carbon nanofibres growth [20].

* Corresponding author. Tel.: +34 91 488 80 96; fax: +34 91 488 70 68.
E-mail address: arturo.vizcaino@urjc.es (A.J. Vizcaíno).

0920-5861/$ – see front matter © 2008 Elsevier B.V. All rights reserved.
doi:10.1016/j.cattod.2008.11.020

(ii) Increasing the support basic properties in order to hinder reactions catalyzed by acid sites such as ethanol dehydration to ethylene and so decreases carbon formation [21,22].

The first strategy may be accomplished by the use of supports with appropriate textural properties. In this sense, mesostructured materials have shown good characteristics for accommodating metallic particles [23,24] due to their controllable pore size, pore volume, and high surface area. In previous works [8,9], we have demonstrated the better performance of siliceous SBA-15 material, compared to silica, MCM-41, γ-alumina and ZSM-5 zeolite as support of Cu–Ni catalysts.

On the other hand, some authors [10–12,21,22,25–27] have improved catalysts performance on reforming processes by adding alkaline elements, such as K, Mg or Ca in order to reduce catalysts acid sites. Most studies have been done with alumina supported Ni catalysts, where the addition of alkaline-earth elements improved catalyst stability. This was attributed to the reduction of coke formation or even to a retarded Ni sintering by improving the Ni dispersion and strengthening the nickel–alumina interaction [22,27]. The influence of alkaline-earth elements on the activity of supported Ni catalysts depends on the amount added and the properties of the support [22]. Moreover, Cheng et al. [25] described that the promoting effect is more significant when the support is impregnated with the promoter before the incorporation of the active phase.

For these reasons, it has been considered interesting to prepare Cu–Ni catalysts supported on Mg- and Ca-modified SBA-15 mesoporous materials and to test them in the hydrogen production through ethanol steam reforming.

2. Experimental

2.1. Catalysts preparation

SBA-15 support was synthesized by the hydrothermal method described by Zhao et al. [28]. Subsequent air calcination at 550 °C in static conditions for 5 h at a heating rate of 1.8 °C/min was carried out to eliminate the template. Four modified supports were prepared by incipient wetness impregnation of SBA-15 using aqueous solutions of $Mg(NO_3)_3{\cdot}6H_2O$ or $Ca(NO_3)_2{\cdot}6H_2O$ (Aldrich). The concentration of the solutions was suited to obtain Ca and Mg loadings of 10 and 20 wt% after calcination at 550 °C for 5 h. Supports were denoted as *Mx* – SBA, where *M* represents the promoter element (Mg or Ca), *x* indicates the nominal wt% loading and *SBA* refers to the SBA-15 carrier.

The Cu–Ni phase was added by incipient wetness co-impregnation of the corresponding support with aqueous solutions of $Ni(NO_3)_2{\cdot}6H_2O$ and $Cu(NO_3)_2{\cdot}3H_2O$ (Scharlab) with the proper concentration to obtain 7 wt% Ni and 2 wt% Cu loadings in the catalysts, selected on the basis of a previous work [9]. These materials were dried overnight and calcined at 400 °C for 15 h with a heating rate of 1.8 °C/min. Obtained catalysts were named as CuNi/*Mx* – SBA.

2.2. Supports and catalysts characterization

Characterization analyses were performed by thermogravimetric analyses (TGA), XRD, ICP-AES, N_2 physisorption, TPR and TEM.

TGA measurements were performed in airflow on a TA instruments SDT 2960 thermobalance, with a heating rate of 5 °C/min up to 800 °C.

XRD was used to determine supports porous mesostructure and catalysts crystalline phases (according to the JCPDS index), as well as mean metallic crystallites diameters calculated by Scherrer equation. Data were acquired on a Philips X'Pert PRO diffractometer, using Cu Kα radiation, a 2θ increment step of 0.020° and a collection time of 2 s. The diffractometer is equipped with a high-temperature chamber in order to analyse samples in situ at different temperatures.

ICP-AES was used to determine the actual metal content in the catalysts. Analyses of the samples, previously dissolved by acidic digestion, were performed on a Varian VISTA-PRO AX spectrophotometer.

Textural properties were measured by N_2 adsorption/desorption analyses at 77 K, using a Micromeritics TRISTAR 3000 sorptometer. Prior to the nitrogen-adsorption, samples were outgassed under vacuum at 200 °C for 4 h. Surface areas were calculated according to BET method.

In order to get information about samples reducibility, TPR profiles were obtained on Micromeritics AUTOCHEM 2910 equipment. Sample was placed in a fixed-bed quartz tube and degasified under dry argon flow (35 mL/min) at 110 °C for 30 min with a heating rate of 15 °C/min. Analyses were carried out under 10% hydrogen in argon flow (35 mL/min) with a heating rate of 5 °C/min from 25 to 800 °C. Effluent gas is forced to flow through a cold trap to remove water produced before reaching the TCD detector.

TEM micrographs were obtained on a Philips TECNAI 20 microscope equipped with W filament and an accelerating voltage of 200 kV, with a point-to-point resolution of 0.27 nm. The apparatus has also the possibility to perform elemental microanalysis by energy dispersive X-ray spectroscopy (EDX). Samples were prepared by powder dispersion of the material, finely divided, in acetone and subsequent deposition on a gold grid with a carbon support.

2.3. Catalytic tests

Catalysts were tested for ethanol steam reforming reaction on a Microactivity-Pro unit, as described elsewhere [8,9]. Outlet flow composition was on-line analysed using a gas chromatograph Varian CP-3380 equipped with Hayesep Q and Molecular Sieve 13× columns. The catalyst was diluted with silicon carbide (catalyst/silicon carbide weight ratio 1:5) and in situ reduced under flowing hydrogen (30 mL/min) at 550 °C for 4.5 h with a heating rate of 2 °C/min. Activated catalyst was heated up to 600 °C and, then, catalytic test was carried out isothermally at atmospheric pressure using nitrogen as carrier gas. A liquid reaction mixture water/ethanol = 3.7 molar ratio was introduced at a flow rate of 0.075 mL/min, vaporized at 150 °C and further eluted by nitrogen (30 mL/min). Weight hourly space velocity (WHSV), defined as the ratio between the inlet feed (water + ethanol) mass flow rate and the mass of catalyst, was fixed at 12.7 h^{-1}.

Carbon deposited during reaction was evaluated from mass difference after coke total combustion process by heating the used catalysts in an oven under air static conditions at 550 °C for 15 h. In order to validate the mentioned method, TGA were performed in air flow on a TA instruments SDT 2960 thermobalance, with a heating rate of 5 °C/min up to 800 °C, proving the agreement between both methods. The value of carbon deposition is given as

$$C_{\text{dep}}\,(\text{wt}\%) = \frac{m_{\text{coke}}}{m_{\text{used catalyst}}} \times 100$$

3. Results and discussion

3.1. Characterization of Mg- and Ca-modified SBA-15 supports

In order to study the processes taking place during the calcination of the impregnated Mg- and Ca-modified SBA-15

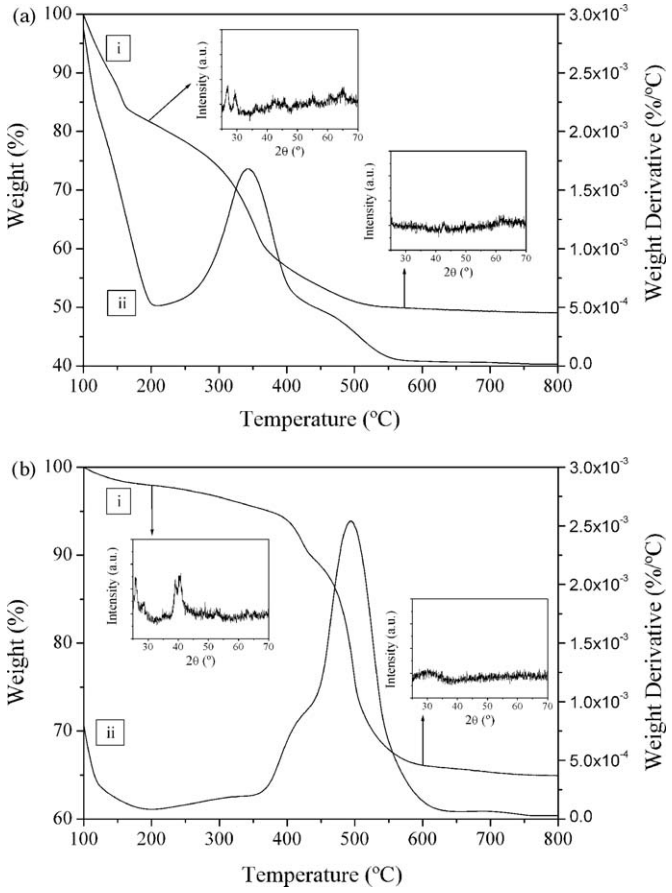

Fig. 1. Thermogravimetric analysis and XRD diffractograms at different calcination temperatures: (a) Mg20-SBA; (b) Ca20-SBA: (i) TG; (ii) DTG.

supports, TGA and XRD analyses were performed. Fig. 1 shows the thermograms obtained with impregnated Mg20-SBA and Ca20-SBA samples. In both cases, a weight loss below 200 °C can be observed and, according to the XRD diffractograms taken at 200 °C, only peaks assigned to the corresponding anhydrous nitrate can be observed (JCPDS 19-0765 and JCPDS 07-0204), so this weight loss may be related to the release of adsorbed and hydration water. At higher temperatures, another wide weight loss can be observed, with maximum drop around 343 °C for Mg20-SBA and 493 °C for Ca20-SBA sample. Although no Mg or Ca species could be detected by XRD even after calcination at 575–600 °C, taking into account the weight percentage drop detected by TGA, this loss is attributed to the anhydrous nitrates decomposition towards the corresponding oxides, as it matches up with the theoretical value calculated from the Mg and Ca contents measured by ICP-AES (see Table 1). This indicates that CaO and MgO crystallites formed over SBA-15 mesoporous support are too small to be detectable by XRD.

Table 1
Physicochemical properties of calcined Mg- and Ca-SBA-15 supports.

Support	Mg or Ca[a] (wt%)	S_{BET} (m^2/g)	V_p[b] (cm^3/g)	D_p[c] (nm)
SBA-15	0.0	678	1.15	10.7
Mg10-SBA	11.0	343	0.76	10.6
Mg20-SBA	19.6	292	0.68	10.1
Ca10-SBA	9.3	304	0.68	10.2
Ca20-SBA	19.1	204	0.50	9.4

[a] ICP-AES measurements.
[b] Determined at $P/P_0 = 0.98$.
[c] Calculated through the maximum of the BJH pore size distribution.

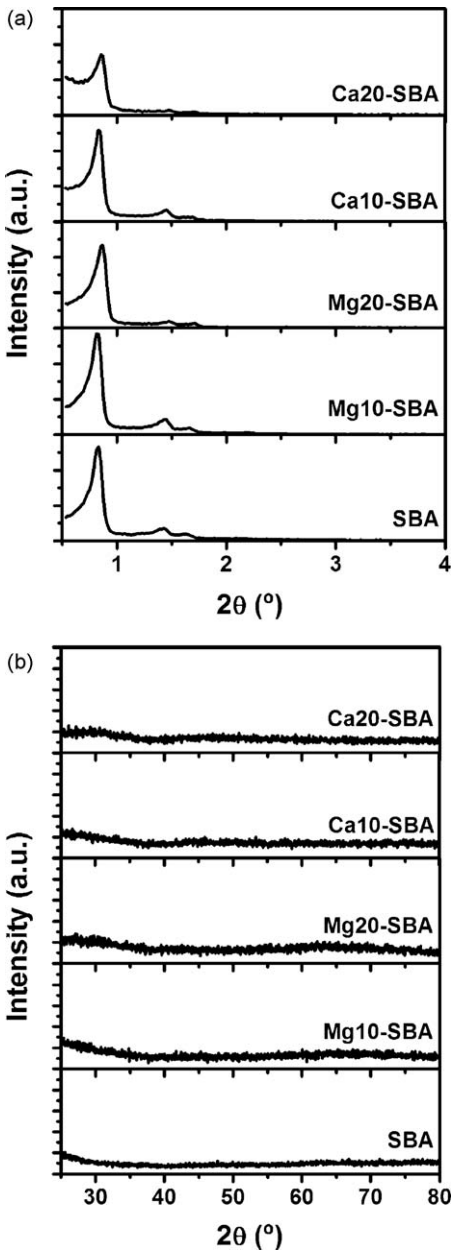

Fig. 2. X-ray difractograms of Mg- and Ca-modified SBA-15 supports: (a) low angle; (b) high angle.

Fig. 2 shows XRD patterns of calcined Mg- and Ca-SBA-15 supports. An intense main diffraction peak and two weak peaks can be observed at low angles (Fig. 2.a), corresponding to the (1 0 0), (1 1 0), (2 0 0) planes, characteristics of the hexagonal pore mesostructure of SBA-15 material. This indicates that the structure is well preserved after the promoters incorporation, although the peaks intensity is slightly reduced for Ca20-SBA sample. At high angles (Fig. 2b), it would be expected to find diffraction peaks corresponding to magnesium or calcium oxides produced after calcination at 550 °C. However, the absence of XRD peaks is indicative of a high dispersion of these oxides over the SBA-15 support.

Fig. 3 shows nitrogen-physisorption analyses of Ca- or Mg-modified SBA-15 supports. All these samples exhibited type IV isotherms with a hysteresis loop (Fig. 3a), typical of mesoporous materials, confirming the preservation of the porous structure upon promoters addition. However, nitrogen adsorbed volume decreases with Ca and Mg loading, which suggest some loss of

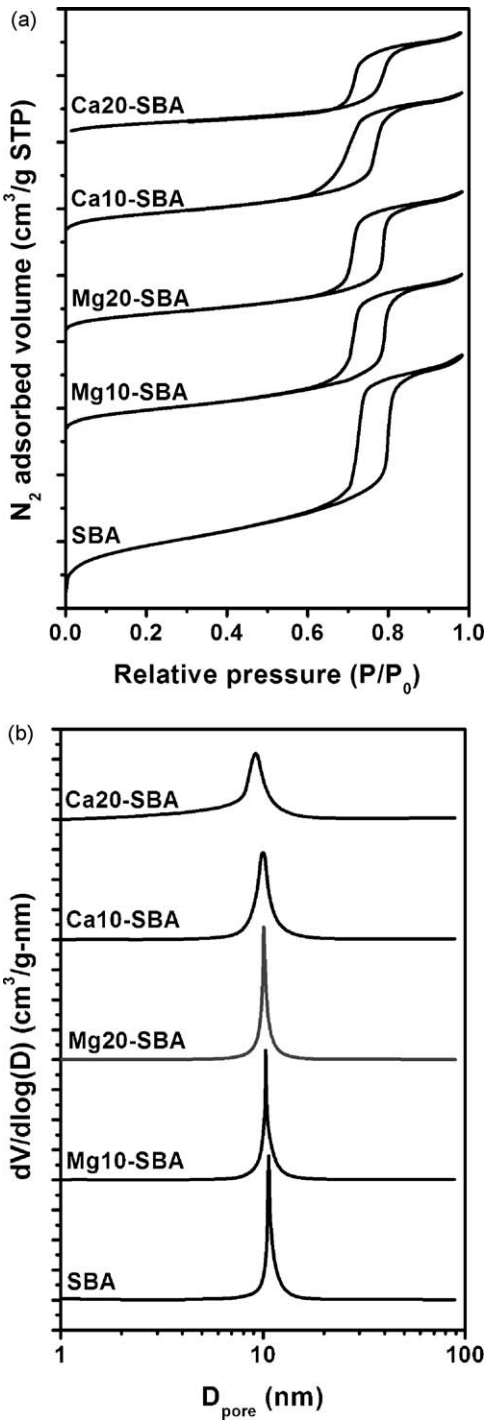

Fig. 3. Nitrogen adsorption–desorption analysis (at 77 K) of Mg- and Ca-modified supports: (a) isotherms; (b) pore size distribution.

porosity due to promoters incorporation. Moreover, supports present a narrow pore size distribution around 10 nm (Fig. 3b), typical of SBA-15 materials. Nevertheless, it is wider for Ca-modified supports, which may be related to a little porous structure distortion by incorporating high amounts of calcium onto the support. Textural properties values are shown in Table 1. Comparing bare SBA-15 with modified supports, it can be observed a significant reduction on the surface area and pore volume by promoters incorporation, without significant changes in pore size. Only Ca20-SBA sample presents narrower pores by the presence of high Ca amounts.

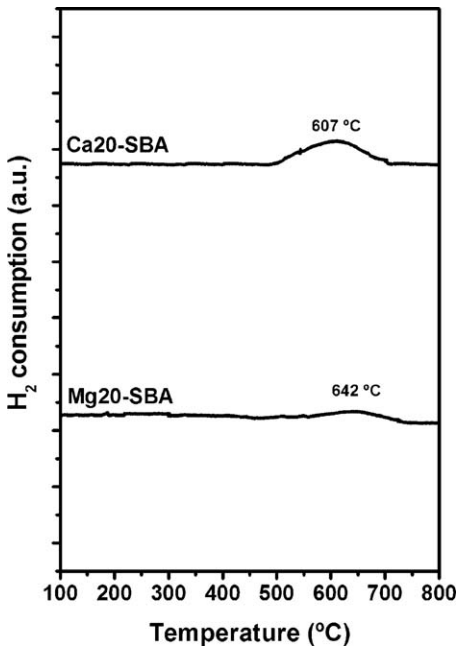

Fig. 4. TPR profiles of Mg- and Ca-modified SBA-15 supports.

In order to study the reducibility of the modified supports, TPR analysis of Mg20-SBA and Ca20-SBA samples were performed and the corresponding profiles are shown in Fig. 4. As it can be seen, Mg20-SBA sample presents a non-significant reduction area around 642 °C, while Ca20-SBA shows a small reduction peak around 607 °C. From the hydrogen consumption calculated through the area under the curves, it has been determined that just 6% and 13% of the total MgO and CaO loading, respectively, have been reduced. This may indicate that only the superficial MgO and CaO can be reduced under these conditions.

3.2. Catalysts characterization

Table 2 summarizes the physicochemical properties of the Cu–Ni catalysts supported on Ca-SBA and Mg-SBA mesoporous materials. In comparison to the corresponding support, it can be observed that the incorporation of Cu (2 wt%) and Ni (7 wt%) reduces surface area and, mainly, pore volume and mean pore diameter. This may indicate some blocking of the support porosity after incorporation of the Cu–Ni phase. As observed for the corresponding supports, catalysts containing 20 wt% of Mg and mainly 20 wt% of Ca present lower textural properties.

Fig. 5 exhibits XRD diffractograms of the calcined Cu–Ni catalysts. Small-angle XRD patterns (Fig. 5a) show the main diffraction peak assigned to (1 0 0) plane reflection, which indicates that the ordered hexagonal mesostructure of Ca or Mg-SBA-15 supports have been well retained on the Cu–Ni catalysts. The XRD patterns at high angle are shown in Fig. 5b. CuNi/SBA sample clearly exhibits peaks at $2\theta = 37.3^\circ$, 43.3° and 62.9°, corresponding to the planes (1 1 1), (2 0 0) and (2 2 0) of cubic NiO (JCPDS 78-0643), respectively, while no CuO peak can be distinguished due to its low loading, as previously reported [9]. Regarding promoted catalysts, it can be found that NiO peaks become wider and almost negligible for Mg-modified samples and even disappear for Ca-promoted catalysts. This is indicative of the formation of smaller NiO crystallites in the presence of magnesium and calcium onto the SBA-15 support. In fact, while the NiO mean crystallite size was 9.4 nm for CuNi/SBA sample, as calculated from the line broadening of the NiO (2 0 0) diffraction using the Scherrer

Table 2
Physicochemical properties of calcined Mg- and Ca-modified CuNi/SBA-15 catalysts.

Catalyst	Cu[a] (wt%)	Ni[a] (wt%)	Mg or Ca[a] (wt%)	S_{BET} (m^2/g)	V_p[b] (cm^3/g)	D_p[c] (nm)
CuNi/SBA	2.0	6.6	0.0	511	0.80	7.9
CuNi/Mg10-SBA	1.9	6.6	10.1	284	0.49	7.9
CuNi/Mg20-SBA	2.0	6.5	17.8	162	0.24	7.7
CuNi/Ca10-SBA	1.7	6.8	8.4	255	0.45	7.6
CuNi/Ca20-SBA	1.9	6.6	17.4	159	0.24	7.5

[a] ICP-AES measurements.
[b] Determined at $P/P_0 = 0.98$.
[c] Calculated through the maximum of the BJH pore size distribution.

equation, poor sharpness of the XRD peaks obtained with promoted samples made it not possible to calculate crystallites size. Moreover, Mg and Ca oxides remain highly dispersed in promoted catalysts, since no peak corresponding to these oxides are observed in the XRD patterns.

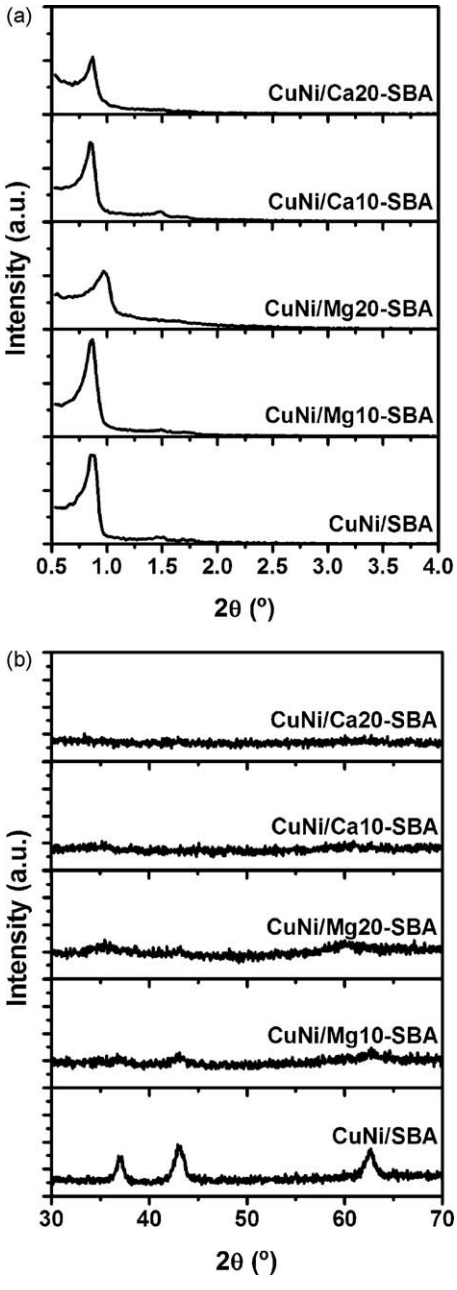

Fig. 5. XRD diffractograms of calcined Mg- and Ca-modified CuNi/SBA-15 catalysts: (a) low angle; (b) high angle.

A similar trend can be observed from the XRD patterns of the reduced samples, shown in Fig. 6. All of them exhibit peaks at $2\theta = 44.5^\circ$ and 51.8°, corresponding to the planes (1 1 1) and (2 0 0) of cubic Ni (JCPDS 04-0850), respectively. Again, no reflection corresponding to any Cu species can be distinguished. Peaks are significantly smaller and wider for the Mg- and Ca-modified catalysts in comparison to the CuNi/SBA sample, which reveals smaller Ni crystallites, as calculated from the line broadening of the Ni (1 1 1) diffraction using the Scherrer equation (values between brackets in Fig. 6).

The improvement of the Cu–Ni phase dispersion by CaO and MgO incorporation onto the catalysts could be verified from TEM micrographs of the calcined samples, shown in Fig. 7. For the CuNi/SBA sample, supported particles (dark zones) can be observed over the mesoporous structure of SBA-15 support (long parallel channels in hexagonal array). EDXS analysis proved the presence of Cu and Ni within each particle, as it was previously reported [8,9]. This catalyst presents CuO–NiO phase crystallites of different sizes, between 5 and 50 nm. Some of them show an irregular shape that seems to adapt to the porous structure of the support, and the other ones show a cubic shape and may be placed over the support external surface. However, for promoted samples, almost no supported particle can be observed in the micrographs. Just for the CuNi/Mg10-SBA sample, some particles of around 5 nm can be scarcely perceived (marked into circles in Fig. 7b). However, EDX analyses demonstrated the presence of copper, nickel and the corresponding alkaline-earth element in the whole samples. This is in accordance with the smaller crystallites size detected by XRD,

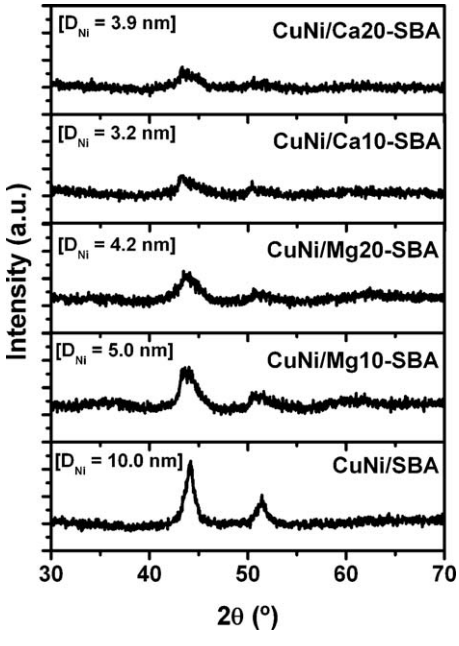

Fig. 6. XRD diffractograms of reduced Mg- and Ca-modified CuNi/SBA-15 catalysts (Ni^0 crystallites sizes calculated from Scherrer equation are shown in brackets).

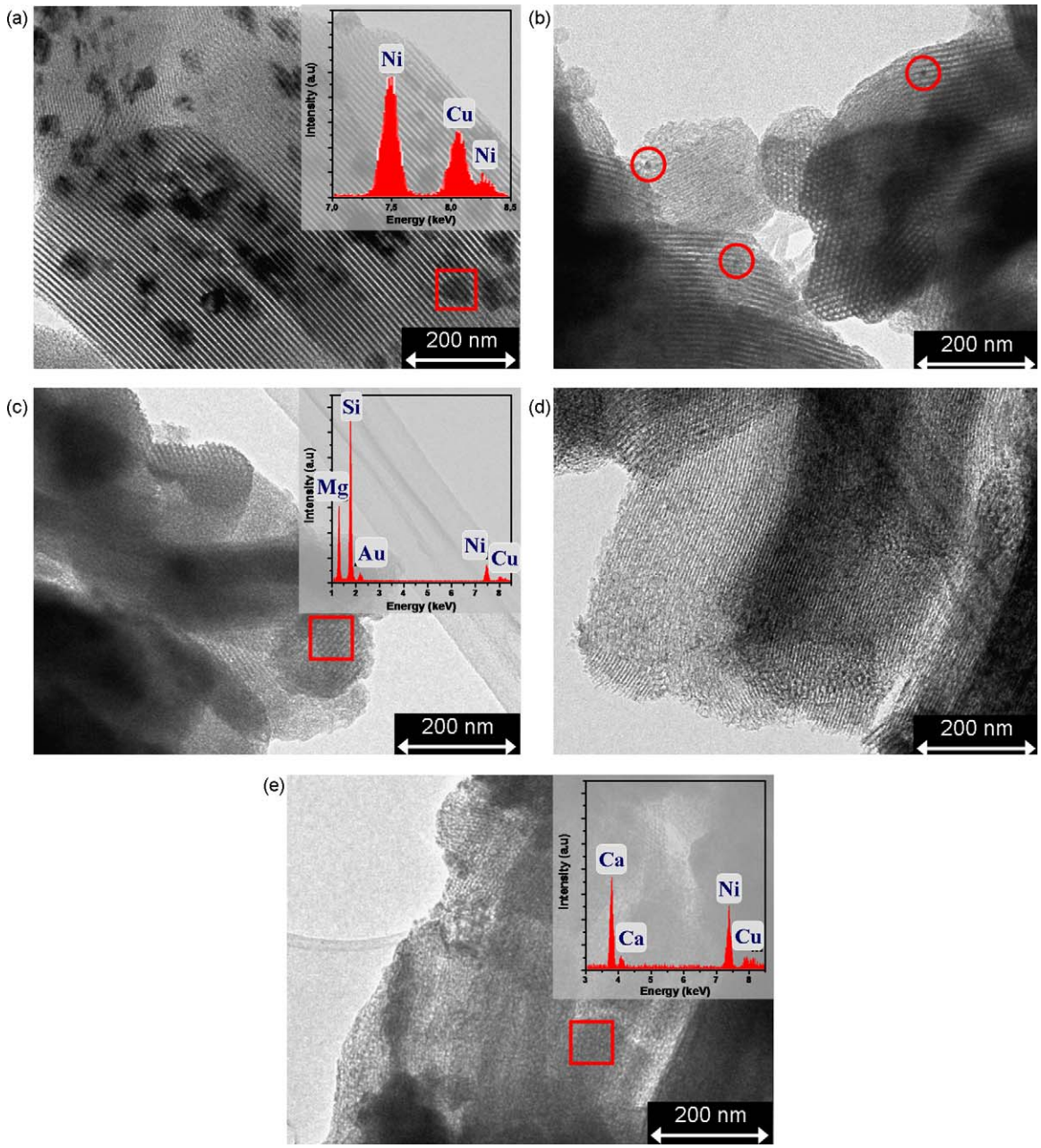

Fig. 7. TEM micrographs of calcined Mg- and Ca-modified CuNi/SBA-15 catalysts: (a) CuNi/SBA, (b) CuNi/Mg10-SBA, (c) CuNi/Mg20-SBA, (d) CuNi/Ca10-SBA and (e) CuNi/Ca20-SBA.

which confirms that high dispersion of the Cu–Ni phase is achieved by incorporating Mg and Ca to the SBA-15 support.

On the other hand, Fig. 8 shows the catalysts TPR profiles. CuNi/SBA sample shows one reduction zone at low temperature, between 150 and 300 °C, made up of two reduction peaks. The main peak at 233 °C corresponds to the reduction of NiO particles supported on SBA-15, while the small one at 180 °C is associated to the reduction of CuO supported particles [8,9]. However, Mg- and Ca-modified catalysts present two reduction zones. At low temperature, below 300 °C, the reduction of CuO and NiO particles with lower metal–support interaction, similar to those observed in CuNi/SBA sample, takes place. On the other side, CuNi/Mg-SBA catalysts show a peak at 503–505 °C assigned to the reduction of copper and nickel oxides strongly bounded to the support. The high temperature reduction zone for CuNi/Ca-SBA catalysts is broader, from 400 to 700 °C, and can be attributed to the overlapped reduction of superficial CaO (see Fig. 4) and a highly stable Cu–Ni phase with strong interaction with the support. By increasing the Ca or Mg loading, the area under the low temperature reduction zone decreases respect to the CuNi/SBA catalyst, while the area under the high temperature reduction zone increases. Thus, the shift of the reduction profile of the SBA-15 supported sample towards higher temperatures for Mg- and Ca-modified catalysts is related to the strengthening of the interaction between the Cu–Ni phase and the support. Moreover, the stronger metal–support interaction in promoted samples agrees with the smaller crystallites sizes found in these catalysts. This effect is slightly more pronounced for Ca than for Mg addition. Almost no difference can be observed between samples containing 10 and 20 wt% loading of the same promoter, except in the case of CuNi/Ca20-SBA sample, where an excess amount of CaO covering the SBA-15 siliceous surface can hinder the metal–support interaction [22].

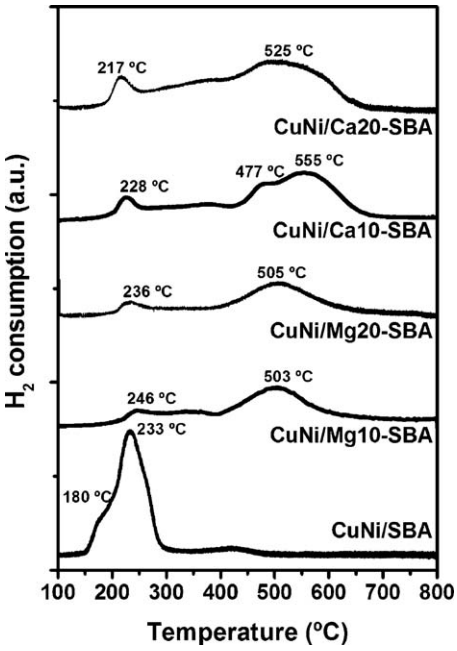

Fig. 8. TPR profiles of Mg- and Ca-modified CuNi/SBA-15 catalysts.

3.3. Catalytic tests on ethanol steam reforming

Fig. 9 shows the catalytic results obtained in ethanol steam reforming at 600 °C. All the catalysts reached complete ethanol conversion under the reaction conditions. Regarding selectivities, significant differences may be observed. In comparison to CuNi/SBA, Mg- and Ca-modified catalysts give small amounts of acetaldehyde in the products stream. On the other side, lower methane selectivity is achieved with promoted samples. This is indicative of higher activity in the methane steam reforming reaction, which is a key step in the ethanol steam reforming mechanism. As a consequence, higher selectivities towards carbon monoxide and main products (hydrogen and carbon dioxide) are reached for both Mg- and Ca-modified catalysts. This behaviour may be attributed to promoting effects of MgO and CaO on the formation of smaller Ni–Cu matrices, as evidenced by XRD and TEM analyses, and the strengthening of the metal–support interaction, observed in TPR profiles. These facts could retard the growth of metallic crystallites by sintering during thermal processes, improving catalysts performance. The increase in

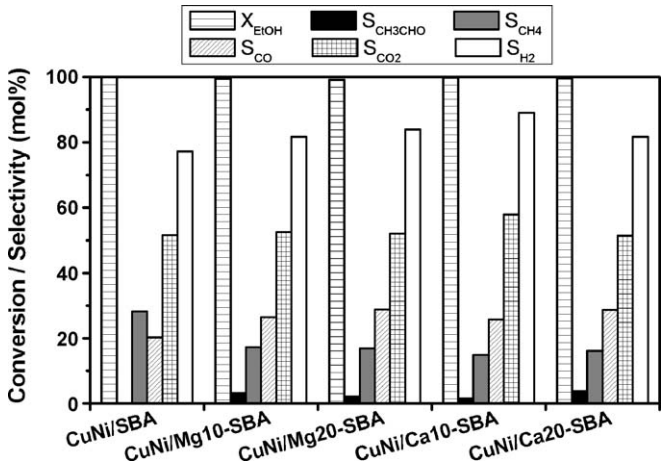

Fig. 9. Catalytic results on ethanol steam reforming reaction using Mg- and Ca-modified CuNi/SBA-15 catalysts.

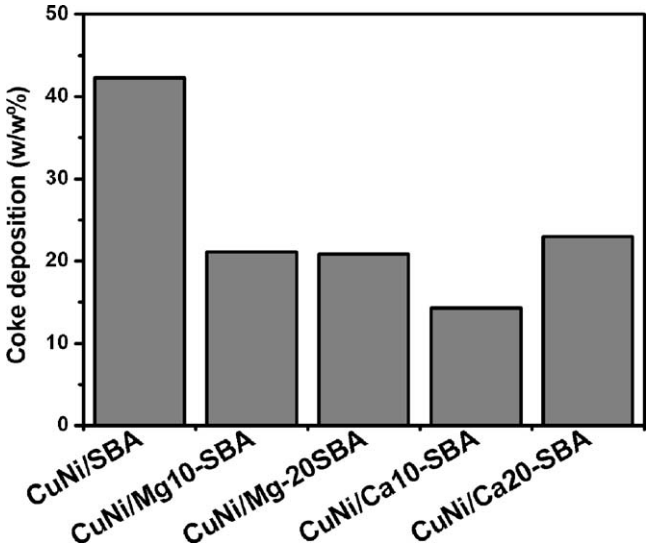

Fig. 10. Coke deposition on used Mg- and Ca-modified CuNi/SBA-15 catalysts after 3 h of time on stream.

carbon monoxide selectivity indicates that the amount formed due to methane steam reforming cannot be totally consumed by water-gas shift reaction. For Mg-modified catalysts, no differences were found in the catalytic behaviour of samples containing 10 or 20 wt% of Mg. However, the highest hydrogen selectivity (89.1 mol%) is achieved with CuNi/Ca10-SBA sample, which exhibits the smallest Ni crystallites (see Fig. 6), while at higher Ca loading the catalyst performance gets worse. This result is in agreement with that obtained by Horiuchi et al. [29] over Ca-modified Ni/γ-Al_2O_3 and may be attributed to the weaker interaction between the Cu–Ni phase and the support when there is an excess of impregnated Ca, as observed from TPR profiles (Fig. 8).

Finally, Fig. 10 compares catalysts in terms of coke formation, measured as weight percentage on the used catalyst after 3 h of reaction time. As it can be observed, in comparison to the CuNi/SBA sample, coke formation was significantly diminished for Mg- and Ca-containing catalysts. This may be attributed to both an increase of support alkalinity, which unfavours the formation of ethylene as intermediate product [21,22], and a decrease of Cu–Ni ensembles size, which negatively affects to the carbon nanofibres formation mechanism [20] and also retards metal sintering. In a similar way as explained above, CuNi/Ca10-SBA sample presents the lowest carbon deposition (14.3, w/w%) due to its high metal dispersion and metal–support interaction, according to XRD, TEM, and TPR analyses, respectively. Thus, with CuNi/Ca10-SBA catalyst, coke deposition has been reduced to almost one third of the amount obtained with CuNi/SBA sample.

4. Conclusions

Magnesium- and calcium-containing CuNi/SBA-15 mesoporous catalysts have been synthesized in order to study the effects of alkaline-earth elements incorporation on their properties and catalytic performance in ethanol steam reforming.

It was found that incorporation of 10–20 wt% of Mg or Ca reduces the metallic phase particles size in Cu–Ni/SBA-15 catalysts and it strengthens metal–support interaction. Both promoting effects of Mg and Ca lead to a better catalytic behaviour of CuNi/SBA-15 catalysts on the ethanol steam reforming process, improving the hydrogen production by an enhancement of the methane steam reforming reaction. Moreover, alkalinity of Mg and Ca, together with smaller Cu–Ni crystallites found on Mg- and Ca-promoted catalysts,

partially inhibits carbon nanofibres formation mechanism, so that lower coke amounts were formed. The best catalytic results, in terms of highest hydrogen selectivity and lowest coke deposition, were reached with a Cu–Ni catalyst supported on SBA-15 mesoporous material doped with 10 wt% of Ca.

References

[1] International Energy Agency, World Energy Outlook 2006, IEA Publications, Paris, 2006.
[2] M. Momirlan, T.N. Veziroglu, Int. J. Hydrogen Energy 30 (2005) 795.
[3] Intergovernmental Panel on Climate Change, Third Assessment Report: Climate Change 2001, Cambridge University Press, New York, 2001.
[4] A. Haryanto, S. Fernando, N. Murali, S. Adhikari, Energy Fuels 19 (2005 2098).
[5] K.A. Gray, L. Zhao, M. Emptage, Curr. Opin. Chem. Biol. 10 (2006) 141.
[6] D.L. Trimm, Catal. Today 37 (1997) 233.
[7] F. Besenbacher, I. Chorkendorff, B.S. Clausen, B. Hammer, A.M. Molenbroek, J.K. Norskov, I. Stensgaard, Science 279 (1998) 1913.
[8] A.J. Vizcaíno, A. Carrero, J.A. Calles, Int. J. Hydrogen Energy 32 (2007) 1450.
[9] A. Carrero, J.A. Calles, A.J. Vizcaíno, Appl. Catal. A: Gen. 327 (2007) 82.
[10] F. Mariño, E.G. Cerrella, S. Duhalde, M. Jobbagy, M. Laborde, Int. J. Hydrogen Energy 23 (1998) 1095.
[11] F. Mariño, M. Boveri, G. Baronetti, M. Laborde, Int. J. Hydrogen Energy 26 (2001) 665.
[12] F. Mariño, G. Baronetti, M. Jobbagy, M. Laborde, Appl. Catal. A: Gen. 238 (2003) 41.
[13] F. Mariño, M. Boveri, G. Baronetti, M. Laborde, Int. J. Hydrogen Energy 29 (2004) 67.
[14] V. Klouz, V. Fierro, P. Denton, H. Katz, J.P. Lisse, S. Bouvot-Mauduit, C. Mirodatos, J. Power Sources 105 (2002) 26.
[15] V. Fierro, V. Klouz, O. Akdim, C. Mirodatos, Catal. Today 75 (2002) 141.
[16] V. Fierro, O. Akdim, C. Mirodatos, Green Chem. 5 (2003) 20.
[17] H.S. Bengaard, J.K. Nørskov, J. Sehested, B.S. Clausen, L.P. Nielsen, A.M. Molenbroek, J.R. Rostrup-Nielsen, J. Catal. 209 (2002) 365.
[18] J. Sun, X. Qiu, F. Wu, W. Zhu, W. Wang, S. Hao, Int. J. Hydrogen Energy 29 (2004) 1075.
[19] S. Cavallaro, Energy Fuels 14 (2000) 1195.
[20] H.W. Chen, C.Y. Wang, L.T. Tseng, P.H. Liao, Catal. Today 97 (2004) 173.
[21] J.S. Lisboa, D.C.R.M. Santos, F.B. Passos, F.B. Noronha, Catal. Today 101 (2005) 15.
[22] Z. Hou, O. Yokota, T. Tanaka, T. Yashima, Appl. Catal. A: Gen. 253 (2003) 381.
[23] D. Trong On, D. Desplantier-Giscard, C. Danumah, S. Kaliaguine, Appl. Catal. A: Gen. 222 (2001) 299.
[24] H. Liu, H. Wang, J. Shen, Y. Sun, Z. Liu, Appl. Catal. A: Gen. 337 (2008) 138.
[25] Z. Cheng, Q. Wu, J. Li, Q. Zhu, Catal. Today 30 (1996) 147.
[26] P. Chen, Z.Y. Hou, X.M. Zheng, Chin. J. Chem. 23 (2005) 847.
[27] M.C. Sánchez-Sánchez, R.M. Navarro, J.L.G. Fierro, Int. J. Hydrogen Energy 32 (2007) 1462.
[28] D. Zhao, J. Feng, Q. Huo, N. Melosn, G.H. Fredrickson, B.F. Chmelka, G.D. Stucky, Science 279 (1998) 548.
[29] T. Horiuchi, K. Sakuma, T. Fukui, Y. Kubo, T. Osakim, T. Mori, Appl. Catal. A 144 (1996) 111.